Journal of Molecular Spectroscopy 267 (2011) 136–143

Contents lists available at ScienceDirect

Journal of Molecular Spectroscopy

journal homepage: www.elsevier.com/locate/jms

Superfluid response of ^4He_N–N_2O clusters probed by path integral Monte Carlo simulations

Lecheng Wang [a], Daiqian Xie [a,*], Hua Guo [b], Hui Li [c,1], Robert J. Le Roy [c], Pierre-Nicholas Roy [c]

[a] Institute of Theoretical and Computational Chemistry, Key Laboratory of Mesoscopic Chemistry, School of Chemistry and Chemical Engineering, Nanjing University, Nanjing 210093, China
[b] Department of Chemistry and Chemical Biology, University of New Mexico, Albuquerque, NM 87131, USA
[c] Department of Chemistry, University of Waterloo, Waterloo, Ontario, Canada N2L 3G1

ARTICLE INFO

Article history:
Available online 11 March 2011

Keywords:
Path integral Monte Carlo simulations
Superfluidity
van der Waals clusters

ABSTRACT

Using an improved path integral Monte Carlo method, finite-temperature structural and dynamical properties of ^4He_N–N_2O clusters ($N \leqslant 40$) are investigated. The simulations employed a newly developed He–N_2O interaction potential obtained at the CCSD(T) level. Good agreement with experimental observations was obtained for the evolution of the effective rotational constant as a function of cluster size. In particular, the experimentally observed turnaround at $N = 6$ for the effective rotational constant B_{eff} is attributed to filling of the "donut" ring structure around the equator of the linear impurity molecule, and a second extremum in B_{eff} for cluster sizes near $N = 10$ is associated with the emergence of superfluidity of the quantum solvent. A careful comparison with properties of He_N–CO_2 clusters suggests that the difference between the renormalized rotational constants of the two impurity molecules is due to the anisotropy of the solute–solvent interaction potential.

1. Introduction

Spectroscopic studies of impurity molecules embedded in low-temperature He clusters have revealed fascinating structural and dynamical behaviors of the micro-solvation environment [1]. For example, a linear impurity molecule (OCS) was found to have microwave spectra resembling a free rotor (albeit with a significantly smaller rotational constant) in low-temperature ^{4}He nanodroplets ($N \sim 10^4$), but it undergoes hindered rotation in ^{3}He droplets around the same temperature [2]. This striking observation was taken as evidence for a microscopic manifestation of superfluidity in ^{4}He droplets, apparently due to the exchange of the identical bosonic solvent atoms. This is a unique quantum mechanical phenomenon that has no classical counterpart.

A key question is concerned with the onset of microscopic superfluidity in such clusters. To this end, several infrared and microwave studies have been carried out to probe the micro-solvation environment for linear molecules (OCS, CO_2, and N_2O) embedded in relatively small ^{4}He clusters ($N < 100$) [3–13]. The variation of spectroscopic properties with the size of the cluster provided valuable information on the transition from a simple van der Waals complex to a quantum solution. Most interestingly, strong evidence has been presented for the emergence of superfluidity with only a few ^{4}He atoms.

A remarkable observation was made by Nauta and Miller [14], who found that in ^{4}He nanodroplets the rotational constant of N_2O was just half of CO_2, even though the gas phase constants of the two are similar. The drastically different behaviors of the two chromophores in ^{4}He clusters reflect the sensitivity of spectroscopy to the nature of the interaction between the solvent and impurity. Thus, an accurate dimer potential energy surface (PES) is particularly desirable for understanding the differences in solvation behavior. While elaborate He–CO_2 PESs have been reported by several groups [15,16], of those for He–N_2O [17–19], only one [20] incorporates explicit dependence on the N_2O internal modes. Such dependence is essential for simulating the IR spectra of the N_2O chromophore in such clusters.

With an accurate He–N_2O PES, the spectroscopy of a N_2O molecule embedded in ^{4}He clusters of various sizes can be simulated. To this end, an efficient quantum simulation method is needed to describe quantum fluctuation in these relatively large systems at finite temperatures. An ideal approach is the path integral Monte Carlo (PIMC) method [21], which has been extensively used to investigate doped ^{4}He clusters, yielding rich insights [22,33]. In particular, the ^4He_N–N_2O system has been studied by PIMC [9,25], as well as by other quantum methods [25,34,35]. This work uses the PIMC method developed by Blinov and Roy, which explicitly considers the rotational degree of freedom of the chromophore

* Corresponding author.
E-mail address: dqxie@nju.edu.cn (D. Xie).
[1] Present address: Institute of Theoretical Chemistry, State Key Laboratory of Theoretical and Computational Chemistry, Jilin University, 2519 Jeifang Road, Changchun 130023, People's Republic of China.

0022-2852/$ - see front matter © 2011 Elsevier Inc. All rights reserved.
doi:10.1016/j.jms.2011.03.007

impurity [26,27,36]. The Bose identical-particle exchange was handled using the efficient worm algorithm [37,38].

The paper is organized as follows. Section 2 presents a brief description of the *ab initio* calculation of the He–N_2O PES, and of how it is fitted to an analytic function. Section 3 outlines the PIMC approach for doped ^{4}He clusters, and describes the framework of the superfluidity simulations. Section 4 then presents tests of the PES and the results of our PIMC simulations, together with an analysis of the evolution of the cluster structure and superfluid behavior with cluster size, and a comparison between the properties of ^4He_N–N_2O and ^4He_N–CO_2 clusters. Finally, brief conclusions are presented in Section 5.

2. He–N_2O dimer potential energy surface

Following our earlier work [20], we treated He–N_2O as a three dimensional system whose coordinates were the distance R between He and the center of mass of N_2O, the associated Jacobi angle θ, and the N_2O monomer antisymmetric stretch coordinate Q_3. (The normal coordinates Q_1 and Q_3 are determined by diagonalizing the vibrational Hamiltonian.) The explicit inclusion of Q_3 is designed to allow for realistic simulations of IR spectra of the clusters; however, the present work focuses on their rotational dynamics.

The *ab initio* calculations were based on a direct-product coordinate grid. Specifically, the following 22 point R grid was used: R = 3.6, 4.0, 4.5, 5.0, 5.2, 5.4, 5.6, 5.8, 6.1, 6.4, 6.8, 7.2, 7.6, 7.8, 8.0, 8.3, 8.6, 9.0, 10.0, 13.0, 15.0, and 19.0 Bohr. The grid points at large R are necessary to define the long-range interaction potential that is important for large clusters. In the θ coordinate, twelve points were evenly distributed between 0° and 180°, while five points were employed to describe the antisymmetric stretch Q_3. With a few more points added in the potential well region, a total of 1640 *ab initio* grid points were generated. The electronic structure calculations were carried out with the MOLPRO package [39] at the coupled-cluster singles and doubles level with non-iterative inclusion of connected triples, CCSD(T) [40], with the augmented correlation-consistent quadruple-zeta (AVQZ) basis set [41] being used for all atoms, and this basis was supplemented with bond functions (3*s*3*p*2*d*1*f*1*g*) (for 3*s* and 3*p*, α = 0.9, 0.3, 0.1; for 2*d*, α = 0.6, 0.2; for *f*, α = 0.3) [42] located at the center of the van der Waals bond. A supermolecular approach was adopted, and the full counterpoise procedure [43] was used to correct for basis-set superposition errors.

Following our earlier work [44], we further constructed a two-dimensional (2D) He–N_2O PES for the N_2O ground-state ν_3 level. This was done by averaging the 3D *ab initio* PES with appropriate vibrational wavefunctions:

$$V^{\nu_3}(R,\theta) = \langle \varphi_{\nu_3}(Q_3)|V(R,\theta,Q_3)|\varphi_{\nu_3}(Q_3)\rangle, \tag{1}$$

where $\varphi_{\nu_3}(Q_3)$ is the ν_3 vibrational wavefunction for an isolated N_2O molecule. To take account of contributions from the symmetric stretching mode (ν_1) which might be significant, as discussed in a previous work on the He–CO_2 system [33], we have calculated $\varphi_{\nu_3}(Q_3)$ using the average Q_1 value for ground state N_2O. In particular, for the ν_3 = 0 wavefunction, Q_1 was fixed at a value determined by the average N–N and N–O bond lengths of 1.12872 Å and 1.18792 Å, respectively.

Following the previous study on the potential fitting of He–N_2O [17], the 2D PESs were fitted to the analytical form:

$$V_{\mathrm{He-N_2O}}(R,\theta) = V_{sh}(R,\theta) + V_{as}(R,\theta), \tag{2}$$

in which $V_{sh}(R,\theta)$ is the short-range part with the following form:

$$V_{sh} = G(R,\theta)e^{D(\theta)-B(\theta)R}. \tag{3}$$

The functions D, B and G were expanded in terms of Legendre polynomials $P_l(\cos\theta)$:

$$G(R,\theta) = R^{-2}\sum_{i=0}^{N} R^i \sum_{l=0}^{L_G} g_i^l \frac{P_l(\cos\theta)}{\sqrt{2l+1}}, \tag{4}$$

$$D(\theta) = \sum_{l=0}^{L} d^l \frac{P_l(\cos\theta)}{\sqrt{2l+1}}, \tag{5}$$

$$B(\theta) = \sum_{l=0}^{L} b^l \frac{P_l(\cos\theta)}{\sqrt{2l+1}}, \tag{6}$$

with expansion lengths L = 4, L_G = 5, and N = 4.

The long-range asymptotic term $V_{as}(R,\theta)$ was given in the Tang–Toennies form [45], which includes a damping term for small R:

$$V_{as} = \sum_{i=6}^{12}\left(\frac{f_i[B(\theta)R]}{R^i}\sum_{l=0}^{L_{\max}} C_i^l \frac{P_l(\cos\theta)}{\sqrt{2l+1}}\right), \tag{7}$$

with $f_i(x) = 1 - e^{-x}\sum_{k=0}^{i} x^k/k!$. This analytical potential form was suggested by Tang and Toennies, and modified by Bukowski and coworkers by introducing anisotropy [46]. The fitting was based on the Levenberg–Marquardt nonlinear fitting algorithm [47]. The parameters in the previous work [17] were used as initial guesses for our fit, and the expansion lengths were extended gradually.

3. Path integral Monte Carlo method

3.1. Hamiltonian

The Hamiltonian for the He_N–N_2O cluster may be written as:

$$\hat{H} = \hat{H}_{\mathrm{He}} + \hat{H}_{\mathrm{N_2O}} + V_{\mathrm{He_N N_2O}}, \tag{8}$$

where

$$\hat{H}_{\mathrm{He}} = \sum_{i=1}^{N}\frac{\mathbf{p}_i^2}{2m_{\mathrm{He}}} + \sum_{i<j} u(|\mathbf{r}_i - \mathbf{r}_j|) \tag{9}$$

denotes the Hamiltonian for He atoms with $\mathbf{p}_i$ and $\mathbf{r}_i$ ($i \neq 0$) being the momentum and position of a He atom, respectively. The He–He pair potential u is that of Aziz et al. [48].

The Hamiltonian for the impurity (i = 0) treats it as a translating rigid rotor:

$$\hat{H}_{\mathrm{N_2O}} = \frac{\mathbf{p}_0^2}{2m_{\mathrm{N_2O}}} + B_{\mathrm{N_2O}}\mathbf{L}^2, \tag{10}$$

where $\mathbf{p}_0$ and $\mathbf{L}$, respectively, denote the linear and rotational angular momentum of N_2O. The rotational constant for N_2O is $B_{\mathrm{N_2O}} = 0.4190110\ \mathrm{cm}^{-1}$ [49]. Finally, the interaction potential between He atoms and N_2O is also assumed to be a pairwise sum:

$$V_{\mathrm{He_N N_2O}} = \sum_i V_{\mathrm{He-N_2O}}(R_i,\theta_i), \tag{11}$$

where R_i and θ_i are the Jacobi coordinates of the ith helium atom with respect to the molecular dopant.

3.2. Path integral Monte Carlo

For any quantum mechanical operator ($\hat{O}$), its canonical average can be calculated as follows [21]:

$$\begin{aligned}\langle\hat{O}\rangle_\beta &= \frac{1}{Z}\mathrm{Tr}\{\hat{O}\hat{\rho}(\beta)\}\\ &= \frac{1}{Z}\int d\mathbf{q}d\mathbf{q}'d\mathbf{\Omega}d\mathbf{\Omega}'\langle\mathbf{q}\mathbf{\Omega}|\hat{O}|\mathbf{q}'\mathbf{\Omega}'\rangle\langle\mathbf{q}'\mathbf{\Omega}'|\hat{\rho}(\beta)|\mathbf{q}\mathbf{\Omega}\rangle,\end{aligned} \tag{12}$$

where $Z = \mathrm{Tr}\{\hat{\rho}(\beta)\}$ is the partition function and $\beta = 1/k_BT$. The above integration is performed over the translational coordinates

of both N_2O and He moieties, denoted as $\mathbf{q} = (\mathbf{r}_0, \{\mathbf{r}_{i>0}\})$, and the orientation of N_2O in the space-fixed frame, denoted as Ω.

To compute the density matrix, we adopt the path integral approach [50], in which the integral is discretized in imaginary time:

$$\langle \mathbf{q}'\boldsymbol{\Omega}'|e^{-\beta\widehat{H}}|\mathbf{q}\boldsymbol{\Omega}\rangle = \int\cdots\int \prod_{k=2}^{K'} d\boldsymbol{\Omega}_k \prod_{k=2}^{K} d\mathbf{q}_k \times \prod_{k=1}^{K'} \langle \Omega_k|e^{-\tau'\widehat{T}^{\mathrm{rot}}_{N_2O}}|\Omega_{k+1}\rangle \prod_{k=1}^{K} \left\langle \mathbf{q}_k|e^{-\tau\widehat{H}^{\mathrm{tr}}}|\mathbf{q}_{k+1}\right\rangle \quad (13)$$

where $\widehat{T}^{\mathrm{rot}}_{N_2O}$ represents the rotational kinetic energy operator of N_2O, and $\widehat{H}^{\mathrm{tr}}$ stands for the remainder of the Hamiltonian in Eq. (8). Note that the Trotter time slices are defined separately for transitional and rotational degrees of freedom: $\tau = \beta/K$ and $\tau' = \beta/K'$ [26]. In addition, boundary conditions are defined as $(\mathbf{q}_1\boldsymbol{\Omega}_1) = (\mathbf{q}'\boldsymbol{\Omega}')$ and $(\mathbf{q}_{K+1}\boldsymbol{\Omega}_{K'+1}) = (\mathbf{q}\boldsymbol{\Omega})$.In the PIMC simulation, a closed form [51] was used for the rotational density matrix, while the primitive approximation was employed for the translational density matrix. The sampling for the rotational degree of freedom was performed with the standard Metropolis algorithm [51,52], while that for the translational degrees of freedom was carried out using a multilevel Metropolis algorithm [21]. The Bose exchange was included in PIMC by the efficient worm algorithm [37,38]. The details of the implementation will be presented separately in the near future [53].

3.3. Superfluidity

The Feynman path integral provides a useful framework for the investigation of superfluidity in a bosonic system. In the so-called two-fluid model [9,23,29,54], the solvent density is separated into two components, the superfluid and normal-fluid densities. Linear response theory allows the calculation of the superfluid fraction for rotation parallel (//) or perpendicular (⊥) to the molecular axis of the impurity [55]:

$$f^s_{//(\perp)} = \frac{4m^2_{\mathrm{He}}\langle(\mathbf{A}\cdot\mathbf{n}_{//(\perp)})^2\rangle}{\beta\hbar^2 I^{cl}_{//(\perp)}}, \quad (19)$$

where $I^{cl}_{//(\perp)}$ is the classical moment of inertia. The unit vector parallel (//) or perpendicular (⊥) to the molecular axis of the impurity, $\mathbf{n}_{//(\perp)}$, is defined at the time slice $\tau = 0$. The path area

$$\mathbf{A} = \frac{1}{2}\sum_i \sum_k \left[\mathbf{r}^k_i \times \mathbf{r}^{k+1}_i\right] \quad (20)$$

is related to the positions of the ith solvent atom at the imaginary time slices k and $k+1$, $\mathbf{r}^k_i$ and $\mathbf{r}^{k+1}_i$.

Within the two-fluid model, the renormalization of the rotational constant is considered as the drag of the normal component of solvent atoms by a rotating impurity molecule, and the remaining atoms at superfluid state do not contribute to the moment of inertia. Thus, the expression for the moment of inertia contributed by the solvent atoms in the normal state $I^n_{//(\perp)}$ is:

$$I^n_{//(\perp)} = I^{cl}_{//(\perp)}\left(1 - f^s_{//(\perp)}\right). \quad (21)$$

Denoting the moment of inertia of the impurity molecule as I^{imp}, the total moment of inertia of the solvent–molecule complex can be expressed as $I_\perp \approx I^{imp} + I^n_\perp$ and $I_{//} = I^n_{//}$ [9]. It is clear that in the superfluid limit ($f^s_\perp = 1$) the perpendicular moment of inertia is dominated by that of the impurity. The effective rotational constant B_{eff} is related to $I_\perp$, and it can be compared with that obtained by directly fitting the canonical orientational correlation function to the PIMC data [26].

4. Results and discussion

4.1. He–N_2O potential energy surface

The 63 fitting parameters defined in Eqs. (2)–(7) for the ν_3 ground state of N_2O are listed in Tables 1 and 2. The good quality of fit is demonstrated by the very small ($\sim$0.004 cm^{-1}) root-mean-square (RMS) deviation from the *ab initio* points at energies below 100 cm^{-1}.

Fig. 1 displays a contour plot of the fitted He–N_2O PES for $\nu_3 = 0$. A T-shaped global minimum with an energy of −62.27 cm^{-1} is located at $R = 2.983$ Å and $\theta = 87.02°$, and a collinear minimum with an energy of −32.81 cm^{-1} is located at $R = 4.13$ Å with the He attached to the O end of the molecule. The energy minima are close to those reported in our earlier work (−62.34 and −32.88 cm^{-1}), which used the same CCSD(T) level of theory with smaller AVTZ basis set [20].

Table 1
Parameters defining the short-range portion $V_{sh}(R,\theta)$ of the He–N_2O potential.

l	0	1	2	3	4	5
d^l	141209.516630	−1.66670463	6.79863607	−0.56726561	1.10422416	
b^l (Å^{-1})	3.15958096	0.00994087	0.74106730	−0.04225818	0.26650407	
g^l_0(Å^{2}cm^{-1})	367.16631696	−397.04482027	262.75247753	−1236.05919011	−3208.80538543	−866.35752497
g^l_1(Åcm^{-1})	−966.93756842	−382.62982168	−1846.21051731	957.33264866	4832.56339672	1348.32204428
g^l_2(cm^{-1})	873.82520979	901.13038957	1587.87452510	−123.74423496	−2682.35640556	−845.09048111
g^l_3(cm^{-1}/Å)	−262.60894310	−339.09804866	−430.49558742	−20.53157619	632.15318956	222.48747006
g^l_4(cm^{-1}/Å^2)	39.22456940	51.32272582	16.88199791	−10.27419674	−52.16452842	−19.26104499

Table 2
Parameters C^l_n(Å^{n}cm^{-1}) defining the long-range portion $V_{as}(R,\theta)$ of the He–N_2O potential: $l = 0, 2, 4, 6, 8$ for even values of n and $l = 1, 3, 5, 7$ for odd n.

l	0/1	2/3	4/5	6/7	8
C^l_6	7.915762E + 03	−3.496429E + 04			
C^l_7	4.575543E + 04	1.147595E + 05			
C^l_8	−1.312085E + 07	−3.153534E + 06	6.931970E + 05		
C^l_9	4.622296E + 06	−9.015936E + 06	−3.844723E + 05		
C^l_{10}	6.667501E + 08	−2.810092E + 07	−1.308070E + 08	3.151062E + 05	
C^l_{11}	−4.229494E + 07	3.012443E + 08	4.500103E + 07	−1.332789E + 06	
C^l_{12}	−1.335133E + 10	4.055772E + 08	3.977583E + 09	−7.648456E + 07	−7.173112E + 07

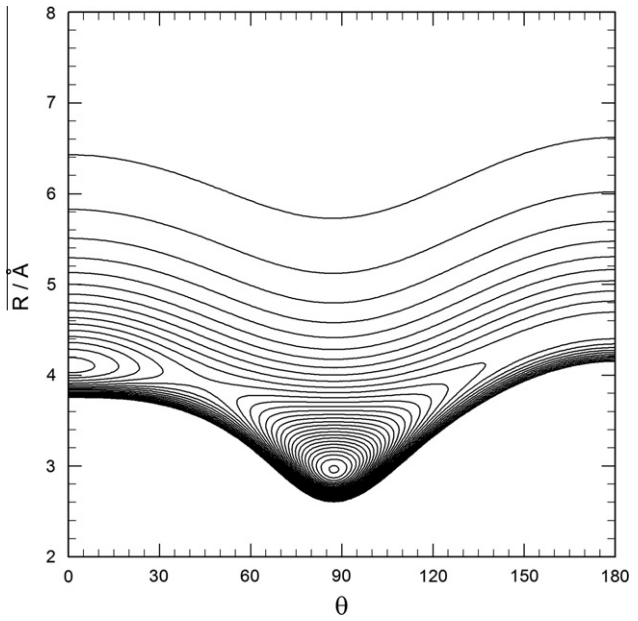

Fig. 1. Contour plot of the fitted He–N_2O potential energy surface (for $v_3 = 0$) as a function of R and θ. The angles $\theta = 0$ and π, respectively, correspond to the oxygen and nitrogen ends of the impurity. The contours descend from 0 to -62 cm^{-1} with an interval of 2 cm^{-1}.

To assess the accuracy of the He–N_2O PES, we have computed a number of transition energies between pure rotational levels of the He–N_2O van der Waals complex by the discrete variable representation (DVR) method [56–58] and compared them with experiment. As shown in Table 3, the errors in the transition energies calculated from the present PES are slightly smaller than those obtained from the surface reported in Ref. [19].

4.2. PIMC

4.2.1. Numerics

The main source of systematic errors in a PIMC simulation is the "primitive approximation", that is, the finite number of time slices used in actual calculations. Extensive convergence tests have thus been performed with respect to the number of time slices in both the rotational and translational degrees of freedom. It was found that 512 translational and 128 rotational time slices are sufficient to converge the results. The PIMC simulations were performed at $T = 0.37$ K. The number of Monte Carlo steps was of the order of 10^8.

Table 3
Comparison of calculated rotational transition frequencies (in MHZ) with observed ones. The observed frequencies v_{obs} denoted by a* symbol came directly from microwave experiments [19] while the others were generated by taking differences between observed infrared transitions [64].

$J'_{K'_aK'_c} - J_{K_aK'_c}$	v_{obs}	v_{cal}[a]	% error[a]	v_{cal}[b]	% error[b]
2_{20}–2_{21}	5184	5044	−2.71	5024	−3.09
1_{10}–1_{11}	6295*	6235	−0.95	6226	−1.10
1_{10}–1_{01}	7478*	7513	0.47	7515	0.49
2_{20}–2_{11}	8639	8778.17	1.61	8795	1.81
1_{01}–0_{00}	18561*	18473.11	−0.47	18453	−0.58
2_{11}–2_{12}	18697	18502.97	−1.04	18477	−1.18
2_{11}–2_{02}		18826.45		18796	
1_{11}–0_{00}	19743*	19750.89	0.04	19741	−0.01
2_{21}–2_{12}	22152	22237.46	0.39	22248	0.43
2_{21}–2_{02}	22427	22560.94	0.60	22567	0.62
2_{02}–1_{11}	30564	30399.93	−0.54	30368	−0.64
2_{12}–1_{11}	30838	30723.41	−0.37	30687	−0.49
2_{02}–1_{01}	31725	31677.71	−0.15	31656	−0.22
2_{12}–1_{01}		32001.20		31976	
2_{11}–1_{10}	43234	42991.34	−0.56	42938	−0.68
2_{21}–1_{10}		46725.83		46709	
		Average	−0.28		−0.35
		RMSD	0.98		1.11

[a] Present PES.
[b] PES from Ref. [19].

4.2.2. Structural properties

As shown in Fig. 1, the nearly T-shaped He–N_2O global minimum has a well depth of 62.27 cm^{-1}, which is eight times larger than that for the He–He pair (7.61 cm^{-1}). Moreover, at the collinear minimum and in the region connecting the two minima, this solvent–molecule interaction is still far stronger than the solvent–solvent interaction. As a result, the structures of small clusters will be mainly determined by the He–N_2O interactions. Only after the strongly attractive regions are occupied will the He–He interaction become significant.

As has been observed for other families of He-solvated chromophores (e.g., He_N–OCS [59–61] and He_N–CO_2 [27,33,62]), the first few He atoms form a "donut" structure, occupying equatorial positions around the linear impurity molecule, due to the deep T-shaped He-molecule potential minimum. Once that first ring of five solvent atoms is filled, additional helium atoms start to form a second ring in the region near the terminal O atom of the N_2O impurity, supported by the collinear minimum. This is clearly shown in Fig. 2 by the distributions of the He atoms for $N = 5$–8. For $N > 9$, the ring at the collinear minimum is fully occupied, and the additional helium atoms start to build a ring about the N end of the molecule, and then caps are added and the density fills in. As discussed below, filling the first shell of helium atoms around the impurity molecule is a pre-requisite for superfluidity perpendicular to the molecular axis. As shown in Fig. 2, the impurity molecule becomes fully solvated near $N = 18$, and the second solvation shell starts to form after that. The distributions go to zero at $\theta = 0$ and π due to the angular normalization.

4.2.3. Energetics

The relative stability of the clusters can be characterized by the chemical potential, which is defined as

$$\mu(N) = E(N) - E(N-1), \tag{23}$$

where $E(N)$ is the energy of the He_N–N_2O cluster. As shown in Fig. 3, the chemical potential is large and negative for the first few He atoms, indicating a large energy drop occurs when each additional He atom is added. An abrupt change occurs after the first "donut ring" is completed at $N = 5$. This can be understood by the fact that additional helium atoms only have access to less strongly attractive sites. The $\mu(N)$ curve increases slightly from $N = 6$ to 8, as helium atoms start to occupy the local minimal site at the oxygen side of the impurity, while for larger N values $\mu(N)$ increases gradually as the helium atoms take positions in regions characterized by weaker solute–solvent interactions.

4.2.4. Rotational dynamics and superfluidity

The effective rotational constant of the solvated impurity can be computed using two approaches. In the conventional approach, it is obtained by fitting the rigid-rotor orientational correlation function directly to the PIMC data [26]. Alternatively, it can be computed using the two-fluid model discussed in Section 3.3. In Fig. 4, the calculated B_{eff} values from both approaches are compared with experimental results for ^4He_N–N_2O of different sizes [9,11]. Here, the calculated results are presented in the figure without error bars, since the statistical errors are very small, ranging from 0.0005 cm^{-1} (large clusters) to 0.0027 cm^{-1} (small clusters). The agreement between the calculated rotational constants and

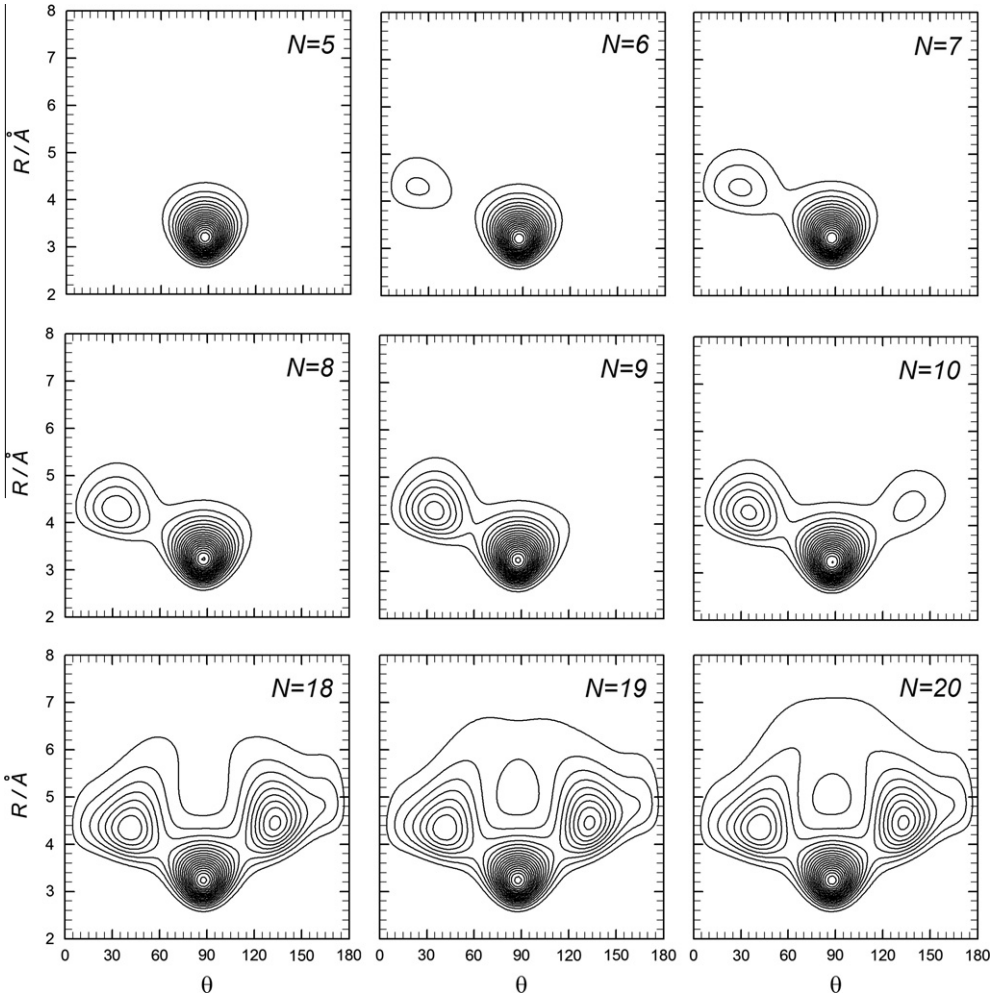

Fig. 2. Averaged distributions of helium atoms around N_2O for $N = 5–10$ and 18–20. The angular weight factor ($\sin\theta$) is included in the plots.

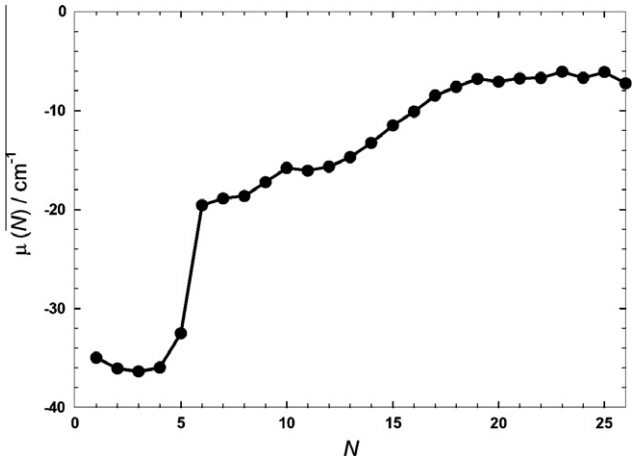

Fig. 3. Calculated chemical potential for He_N–N_2O clusters for $N = 1–26$.

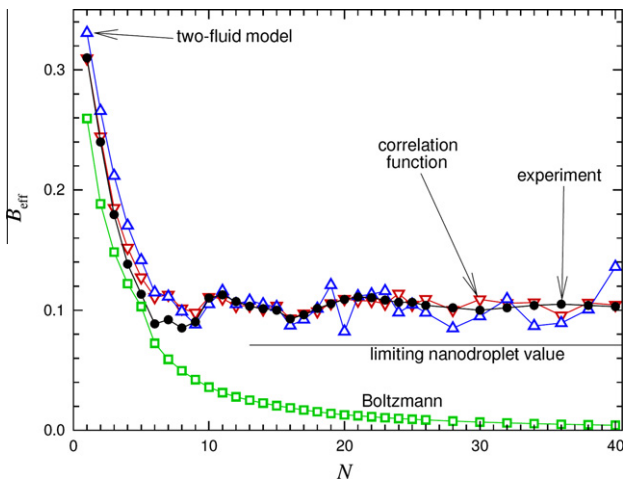

Fig. 4. Rotational constants obtained from fitting to orientation correlation funtions (red gradients) and from the two-fluid model (blue triangles), and their comparison with experimental results from Ref. [11](black solid circles). The corresponding values from Boltzmann simulations (green squares) are included as a benchmark for gauging the effect of bosonic exchange. (For interpretation of the references to color in this figure legend, the reader is referred to the web version of this article.)

the measured ones is quite satisfactory. In particular, the calculated rotational constants reproduce the first turnaround around $N = 6$, as well as the second minimum at $N = 16$. It has previously been suggested theoretically that the effective moment of inertia could increase from $N = 20$ to 30, due to "a new channel of exchanges in the second solvation shell" [25]. However, in agreement with the more recent experimental results [11], our theoretical results show no such increase. Furthermore, the agreement between the PIMC predictions and the experimental results remain excellent for the larger clusters.

It can be seen from Fig. 4 that the agreement with the experimental data is much better for B_{eff} values calculated using the correlation function results than for those obtained from the two-fluid model, for which the results are comparable to those yielded by the earlier work of Xu et al. [9] The differences between the predictions of the two PIMC-based methods could be taken as evidence that the correlation function approach provides a more realistic representation of the rotational dynamics. This may be expected because the two-fluid approach contains additional approximations inherent to linear response theory.

The open square points in Fig. 4 correspond to PIMC correlation-function results obtained while neglecting identical particle bosonic exchange. It is clear that the quantum results start to deviate from this classical Boltzmann behavior for $N > 6$. This deviation of the quantum B_{eff} values from their classical counterparts clearly suggests the emergence of superfluidity stemming from Bose identical-particle exchange. To further understand the superfluid response of the solvent, Fig. 5 shows plots of our calculations of the superfluid fraction in directions parallel and perpendicular to the N_2O axis (see Eq. (19)). The parallel fraction increases rapidly with N and reaches 100% for very small clusters. This implies that for rotation parallel to the molecule axis, the normal moment of inertia vanishes for cluster sizes with $N > 6$, which is confirmed by the lack of a Q-branch in ro-vibrational spectra of doped clusters in this size range [2,9].

Fig. 5 also shows that the superfluid fraction perpendicular to the molecule axis behaves quite differently. Here, our calculated results may be compared with those extracted from experimental determinations of the effective moments of inertia of doped clusters. For cluster sizes $N = 4$–6 both simulation and experiment exhibit a steeper negative slope. This is understandable, as the first few helium atoms increase the effective reduced mass of the rotor. Near $N = 5$, an unambiguous turnaround occurs that suggests the onset of a decoupling between the N_2O rotation and the helium dynamics. As N increases further, the superfluid fraction rises and eventually approaches 100%. This picture is consistent with experimental results shown as solid round points in Fig. 5.

The turnaround shown in Fig. 4 can also be explained by the two-fluid model. In particular, the rise of perpendicular superfluid fraction shown in Fig. 5 leads to a depletion of the normal moment of inertia $I^n_\perp$ for $N > 5$. Consequently, the effective rotational constant of the chromophore stays at roughly the same level, as the superfluid helium atoms contribute negligibly to B_{eff}. Fig. 4 shows that the qualitative agreement between the rotational constants calculated from fitting orientational correlation functions and from the two-fluid model continues to hold for larger clusters, although significant quantitative differences are clearly evident.

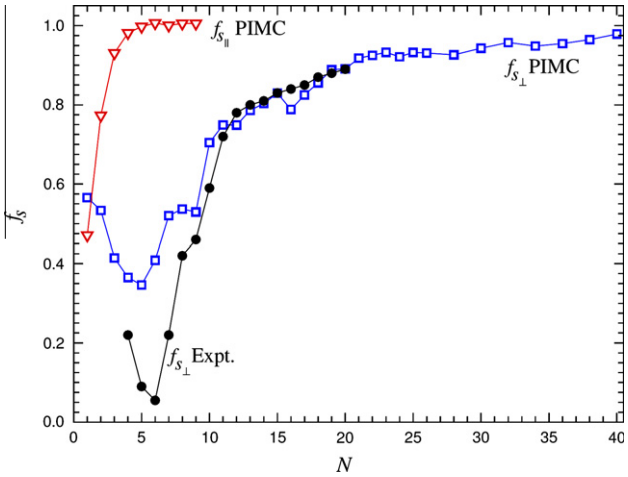

Fig. 5. ^{4}He superfluid fractions of He_N–N_2O clusters perpendicular (blue squares) and parallel (red gradients) to the impurity z-axis. The experimentally derived perpendicular fraction from Ref. [9](black solid circles) are also included for comparison. (For interpretation of the references to color in this figure legend, the reader is referred to the web version of this article.)

4.2.5. Potential function dependence of superfluid behavior

It is interesting to compare the rotational dynamics of the impurity in ^4He_N–N_2O and ^4He_N–CO_2 clusters. As was pointed out earlier, the effective moments of inertia of these two impurity molecules are quite different in ^{4}He clusters, despite the fact that the B rotational constants are quite similar for the isolated molecules. Interestingly, as shown in the inset panel of Fig. 6, the *classical* Boltzmann rotational constants are quite similar for the two clusters, indicating that the difference in B_{eff} behavior is due to quantum Bose exchange. In the upper panel of Fig. 6, the superfluid fraction in the perpendicular direction is plotted for the two clusters as a function of N. It is clear that the transition from normal fluid to superfluid is swift and complete for the ^4He_N–CO_2 clusters with $N > 5$, while that for the ^4He_N–N_2O clusters is much more sluggish. As discussed in Section 3.3, a large superfluid fraction corresponds to a reduced classical contribution of helium atoms to the effective moment of inertia, which explains the smaller B_{eff} for the ^4He_N–CO_2 clusters.

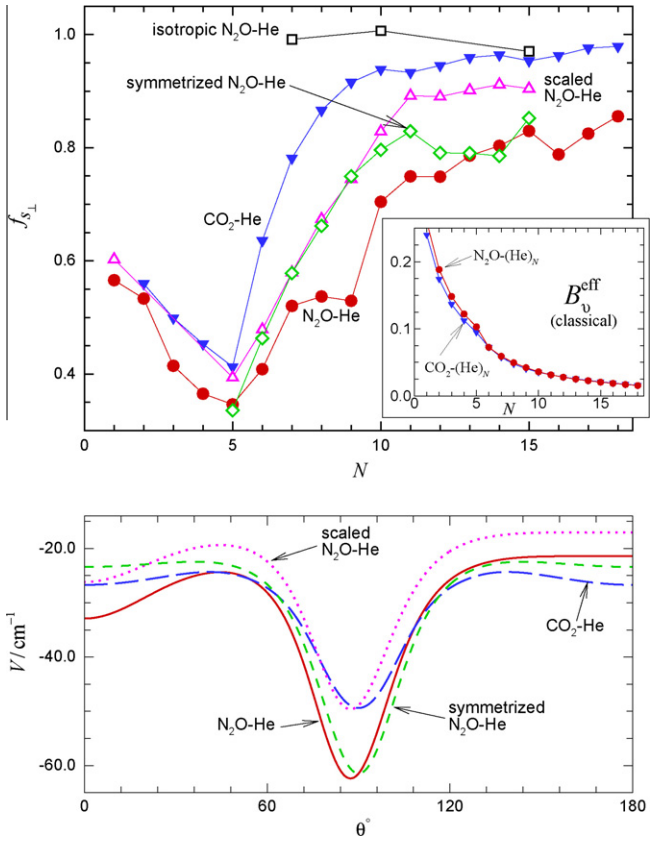

Fig. 6. Upper panel: comparison of the perpendicular superfluid fraction for the He_N–CO_2 (blue solid gradients) and He_N–N_2O clusters (red solid circles). Results for scaled (pink triangles), symmetrized (green diamonds), and isotropic (black open squares) modifications to the He–N_2O PES are also presented (see text for details). The inset compares the classical Boltzmann moments of inertia of the two clusters. Lower panel: angular cuts of the interaction potentials for: He–CO_2 (blue long dashed line); He–N_2O (red solid-line); scaled He–N_2O (pink dotted-line), and symmetrized He–N_2O (green short dashed-line). (For interpretation of the references to color in this figure legend, the reader is referred to the web version of this article.)

The differences in the variation of B_{eff} with N can be attributed to differences in the interaction potential between He and the impurity. Here two factors are particularly important. First, the orientation-dependent potential function wells for the He–N_2O complex are about 20% deeper than those for the He–CO_2 complex, as shown in the lower panel of Fig. 6. A strong solvent–solute interaction generally inhibits solvent exchange, and thus also superfluidity. Indeed, when the strength of the He–N_2O potential is artificially scaled to that of He–CO_2 (purple dotted curve in lower panel), the perpendicular superfluid fraction increases significantly (purple triangle points in upper panel of Fig. 6). However, this increase does not account fully for the differences between the two cases.

Another important factor is the symmetry of the anisotropy of the interaction potential, which is present for He–CO_2 and absent for He–N_2O. In He_N–CO_2, the population of helium atoms near both ends of the impurity grows approximately symmetrically after the donut ring is completed at $N = 5$. This effectively gives rise to a continuous density distribution around the impurity molecule which facilitates the exchange of ^{4}He atoms [31]. As indicated in Eq. (19), the perpendicular superfluid fraction can be expressed as the ratio between the area estimator projected on the direction perpendicular to the impurity molecule axis and its classical counterpart. The area estimator is a sum of cross products between two vectors (Eq. (20)) defined from the impurity center of mass to two different He atoms. As a result, the perpendicular superfluid fraction is dominated by the exchange of helium atoms in the continuous shell around the impurity, and for the normal direction the corresponding area vector is perpendicular to the molecular axis. This can also be understood phenomenologically by the argument that the exchange of helium atoms at the two ends of the impurity is equivalent to rotation of the impurity itself.

For the non-symmetric N_2O, the distribution of helium atoms immediately after the filling of the donut ring at $N = 5$ is asymmetric, and concentrates on the O-atom side of the central donut ring, as shown in Fig. 2. This limits the possibility for the exchange of helium atoms along the length of the N_2O molecule. However, such exchange becomes increasingly possible for $N > 10$, as both the O and N sides of the central ring become populated with helium atoms. The green diamond-shaped points in the upper panel of Fig. 6 present values of the superfluid fraction calculated using a hypothetical He–N_2O potential function that has essentially the correct overall anisotropy, but was artificially symmetrized ($V(\theta) = [V(\theta) + V(\pi - \theta)]/2$; short-dash curve in the lower panel of Fig. 6). It is clear that the enforced artificial symmetry boosts the superfluid fraction values significantly for clusters with $N > 5$, moving them closer to the He_N–CO_2 results. The purple open-triangle points in the upper panel of Fig. 6 were obtained from another modified potential energy surface whose overall anisotropy strength was damped to make it closer to that for He–CO_2 (dotted curve in the lower panel of Fig. 6). It clearly shows a further enhancement in the superfluid fraction for larger ($N > 5$) clusters. Finally, the open square points at the top of Fig. 6 show that a fully isotropic potential with the same overall strength as that of the T-shaped minimum of He–N_2O yields a maximum superfluid response regardless of clusters size. Since such a fully isotropic potential has no angular dependence, no corresponding curve is shown in the lower panel of Fig. 6.

The results shown in Fig. 6 confirm that it is indeed the anisotropy of the interaction potential that causes the inertial drag of the quantum solvent as far as the perpendicular superfluid response is concerned. Although Moroni and coworkers [8,63] had discussed the effect of anisotropy on the effective rotational constants, their ground state simulations could not be used to assess the superfluid response directly. The present analysis therefore complements their findings by making the additional connection to the superfluid response.

5. Conclusions

This work reports an accurate new He–N_2O dimer potential energy surface based on high-level *ab initio* calculations. A reduced-dimension 2D analytic potential energy function was fitted to these results to provide a convenient "working potential" for use in performing simulations. With this accurate potential energy surface, we have carried out finite temperature PIMC simulations of the rotational dynamics of the N_2O embedded in ^{4}He clusters of various sizes. The simulation results are in reasonably good agreement with known experimental data.

A detailed analysis of the superfluid response as a function of cluster size has been performed. It is shown that the calculated effective rotational constant deviates from the classical Boltzmann limit around $N \sim 5$, which indicates the onset of superfluidity in the cluster. This deviation results in a turnaround in the values of the effective rotational constant as a function of N, as has been observed experimentally. This turnaround can also be attributed to the rise of the perpendicular superfluid fraction of the helium atoms, due apparently to Bose exchange. In addition, it is shown that fitting to simulation results for the orientational correlation function gives better predictions of superfluid behavior (better agreement with experiment) than does the two-fluid method, particularly for larger clusters.

Finally, we have elucidated the difference in the nature of the rotational dynamics between a symmetric (CO_2) and asymmetric (N_2O) impurity in ^{4}He clusters. It is shown that the difference in renormalization of the rotational constants of the two helium solvated impurity molecules can be attributed to the anisotropy of the He-impurity interaction potential, which resulted in different onsets of superfluid behavior perpendicular to the molecular axis.

Acknowledgements

LW and DX were supported by the National Natural Science Foundation of China (20725312 and 91021010) and the Ministry of Science and Technology (2007CB815201). HG was supported by Department of Energy (DE-FG02-05ER15694). RJL, HL and PNR acknowledge Natural Sciences and Engineering Research Council of Canada (NSERC), the Canada Foundation for Innovation (CFI), the University of Waterloo, and the Shared Hierarchical Academic Research Computing Network (SHARCNET) for computing time.

References

[1] J.P. Toennies, A.F. Vilesov, Angew. Chim. Int. Ed. 43 (2004) 2622.
[2] S. Grebenev, J.P. Toennies, A.F. Vilesov, Science 279 (1998) 2083.
[3] J. Tang, Y.J. Xu, A.R.W. Mckellar, W. Jaeger, Science 297 (2002) 2030.
[4] Y.J. Xu, W. Jager, J. Tang, A.R.W. McKellar, Phys. Rev. Lett. 91 (2003) 163401.
[5] Y.J. Xu, W. Jäger, J. Chem. Phys. 119 (2003) 5457.
[6] J. Tang, A.W. McKellar, J. Chem. Phys. 119 (2003) 5467.
[7] J. Tang, A.R.W. Mckellar, J. Chem. Phys 121 (2004) 181.
[8] J. Tang, A.R.W. McKellar, F. Mezzacapo, S. Moroni, Phys. Rev. Lett. 92 (2004) 145503.
[9] Y.J. Xu, N. Blinov, W. Jäger, P.-N. Roy, J. Chem. Phys. 124 (2006) 081101.
[10] A.R.W. McKellar, Y.J. Xu, W. Jäger, Phys. Rev. Lett. 97 (2006) 183401.
[11] A.R.W. McKellar, J. Chem. Phys 127 (2007) 044315.
[12] A.R.W. McKellar, Y. Xu, W. Jäger, J. Phys. Chem. A 111 (2007) 7329.
[13] A.R.W. McKellar, J. Chem. Phys. 128 (2008) 044308.
[14] K. Nauta, R.E. Millar, J. Chem. Phys. 115 (2001) 10254.
[15] H. Ran, D. Xie, J. Chem. Phys. 128 (2008) 124323.
[16] H. Li, R.J. Le Roy, Phys. Chem. Chem. Phys. 10 (2008) 4128.
[17] B.T. Chang, O. Akin-Ojo, R. Bukowski, K. Szalewicz, J. Chem. Phys. 119 (2003) 11654.
[18] Y.Z. Zhou, D.Q. Xie, J. Chem. Phys. 120 (2004) 8575.
[19] X. Song, Y.J. Xu, P.-N. Roy, W. Jäger, J. Chem. Phys. 121 (2004) 12308.
[20] Y.Z. Zhou, D.Q. Xie, D.H. Zhang, J. Chem. Phys. 124 (2006) 144317.
[21] D.M. Ceperley, Rev. Mod. Phys 67 (1995) 279.
[22] Y. Kwon, D.M. Ceperley, K.B. Whaley, J. Chem. Phys. 104 (1996) 2341.
[23] Y. Kwon, K.B. Whaley, Phys. Rev. Lett. 83 (1999) 4108.
[24] Y. Kwon, K.B. Whaley, J. Chem. Phys. 115 (2001) 10146.
[25] S. Moroni, N. Blinov, P.-N. Roy, J. Chem. Phys. 121 (2004) 3577.

[26] N. Blinov, X. Song, P.-N. Roy, J. Chem. Phys. 120 (2004) 5916.
[27] N. Blinov, P.-N. Roy, J. Low Temp. Phys. 140 (2005) 253.
[28] R.E. Zillich, F. Paesani, Y. Kwon, K.B. Whaley, J. Chem. Phys. 123 (2005) 114301.
[29] F. Paesani, Y. Kwon, K.B. Whaley, Phys. Rev. Lett. 94 (2005) 153401.
[30] S. Miura, J. Phys.: Condens. Matter 17 (2005) S3259.
[31] S. Miura, J. Tanaka, J. Chem. Phys. 120 (2004) 2160.
[32] S. Miura, J. Chem. Phys. 126 (2007) 114308.
[33] H. Li, N. Blinov, P.-N. Roy, R.J. Le Roy, J. Chem. Phys. 130 (2009) 144305.
[34] F. Paesani, K.B. Whaley, J. Chem. Phys. 121 (2004) 5293.
[35] X.G. Wang, T. Carrington, J. Tang, A.R.W. McKellar, J. Chem. Phys. 123 (2005) 034301.
[36] N. Blinov and P.- N. Roy, (to be published).
[37] M. Boninsegni, N.V. Prokof'ev, B.V. Svistunov, Phys. Rev. Lett. 96 (2006) 070601.
[38] M. Boninsegni, N.V. Prokof'ev, B.V. Svistunov, Phys. Rev. E 74 (2006) 036701.
[39] H.J. Werner, P.J. Knowles, R.D. Amos, D.L. Cooper, M.J.O. Deegan, A.J. Dobbyn, F. Eckert, C. Hampel, T. Leiginger, R. Lindh, A.W. Lloyd, W. Meyer, M.E. Mura, A. Nicklass, P. Palmieri, K.A. Peterson, R. Pitzer, P. Pulay, M. Schutz, H. Stoll, A.J. Stone, T. Thorsteinsson, MOLPRO, version 2006.1, a package of ab initio programs.
[40] K. Raghavachari, G.W. Trucks, J.A. Pople, M. Head-Gordon, Chem. Phys. Lett. 157 (1989) 479.
[41] D.E. Woon, T.H. Dunning, J. Chem. Phys. 98 (1993) 1358.
[42] T.B. Pedersen, B. Fernandez, H. Koch, J. Makarewicz, J. Chem. Phys. 115 (2001) 8431.
[43] S.F. Boys, F. Bernardi, Mol. Phys. 19 (1970) 553.
[44] D.Q. Xie, H. Ran, Y.Z. Zhou, Int. Rev. Phys. Chem. 26 (2007) 487.
[45] K.T. Tang, J.P. Toennies, J. Chem. Phys. 80 (1984) 3726.
[46] R. Bukowski, J. Sadlej, B. Jeziorski, P. Jankowski, K. Szalewicz, S.A. Kucharski, H.L. Williams, B.M. Rice, J. Chem. Phys. 110 (1999) 3785.
[47] W.H. Press, S.A. Teukolsky, W.T. Vetterling, B.P. Flannery, Numerical Recipes, second ed., Cambridge University Press, Cambridge, 1992.
[48] R.A. Aziz, A.R. Janzen, M.R. Moldover, Phys. Rev. Lett. 74 (1995) 1586.
[49] R.A. Toth, J. Opt. Soc. Am. B 4 (1987) 357.
[50] R.P. Feynman, A.P. Hibbs, Quantum Mechanics and Path Integrals, McGraw-Hill, New York, 1965.
[51] D. Marx, M.H. Huser, J. Phys.: Condens. Matter 11 (1999) R117.
[52] N. Metropolis, A.W. Rosenbluth, M.N. Rosenbluth, A.H. Teller, E. Teller, J. Chem. Phys. 21 (1953) 1087.
[53] N. Blinov, H. Li, P.-N. Roy, in preparation.
[54] E.W. Draeger, D.M. Ceperley, Phys. Rev. Lett. 90 (2003) 065301.
[55] P. Sindzingre, M.L. Klein, D.M. Ceperley, Phys. Rev. Lett. 63 (1989) 1601.
[56] J.C. Light, I.P. Hamilton, J.V. Lill, J. Chem. Phys. 82 (1985) 1400.
[57] R. Chen, H. Guo, J. Chem. Phys. 111 (1999) 9955.
[58] H. Guo, R. Chen, D.Q. Xie, J. Theor. Comput. Chem. 1 (2002) 173.
[59] F. Paesani, A. Viel, F.A. Gianturco, K.B. Whaley, Phys. Rev. Lett. 90 (2003) 073401.
[60] F. Paesani, F.A. Gianturco, K.B. Whaley, J. Chem. Phys. 115 (2001) 10225.
[61] S. Moroni, A. Sarsa, S. Fantoni, K.E. Schmidt, S. Baroni, Phys. Rev. Lett. 90 (2003) 143401.
[62] Z. Li, L.C. Wang, H. Ran, D.Q. Xie, J. Chem. Phys. 128 (2008) 224513.
[63] S. Moroni, S. Baroni, Comput. Phys. Commun. 169 (2005) 404.
[64] J. Tang, A.R.W. McKellar, J. Chem. Phys. 117 (2002) 2586.